Surface currents and significant wave height gradients: matching numerical models and high-resolution altimeter wave heights in the Agulhas current region

Gwendal Marechal[1], **Fabrice Ardhuin**[1,2]

[1]Univ. Brest, CNRS, Ifremer, IRD, Laboratoire d'Océanographie Physique et Spatiale, Brest, France
[2]Scripps Institution of Oceanography, University of California, La Jolla, CA, USA

Key Points:

- Spatial resolution of currents is key for reproducing wave height gradients
- 30km resolution over the Agulhas current is necessary to retrieve most of the observed gradients
- Incident waves with a narrow directional spreading induce larger wave height gradients

Corresponding author: Gwendal Marechal, gwendal.marechal@ifremer.fr

Abstract

Advances in the understanding and modelling of surface currents have revealed the importance of mesoscale and submesoscale features. These features should have a large influence on wind waves, and in particular wave heights are expected to be modified by refraction. Still, the quantitative impact of currents on waves is not well known due to the complexity of the random wave fields and currents that are found in the ocean, and the lack of observations of both currents and waves at scales shorter than 150 km. Here we combine novel satellite altimetry data with phase-averaged numerical wave models forced by wind and surface currents fields, taken from the oceanic model CROCO, run at 2.5km resolution. The influence of the spatial resolution of the current field is investigated using smoothed versions of the same current field. We find that a numerical wave model forced with surface currents with resolutions of 30 km or less and a directional resolution of 7.5 degrees or less, can provide accurate representations of the significant wave height gradients found in the Agulhas current. Using smoother current fields, such as derived from satellite measurements of dynamic height, generally underestimates wave height gradients. Hence, satellite altimetry provides high resolution wave height with a gradient magnitude that is a constraint on surface current gradients, at resolutions that may not be resolved by today's combination of mean dynamic topography and altimeter-derived anomalies. Beyond a demonstration for relatively steady currents, this may apply to time-varying currents if enough wave measurements are available.

Plain Language Summary

Mariners have learned to be wary of severe sea states, especially in strong currents like the Agulhas that flows along the South African coast, where wave heights in the current can be several meters taller than in the surrounding waters. Mariners have also learned to spot currents by watching the water ahead of them. Here we use satellite measurements of wave heights and a numerical wave model to understand the parameters that control the spatial variation of wave heights across currents. We particularly question the necessary current magnitude and gradient that are required to explain observed wave height gradients. Modeled gradients fade for smooth surface currents like surface currents estimated from satellite measurements of sea level or typical global ocean circulation models. Also, numerical experiments have shown that when incident waves have a narrow range of directions, wave height gradients are sharper. A good wave model should thus resolve both the current features, with a spatial resolution better than 30 km, and the range of wave directions, typically using 48 directions or more. Such a good model can then be used to evaluate the quality of modeled ocean currents by matching the modeled strength of wave height gradients with measurements.

1 Introduction

Surface gravity waves generated by wind (hereinafter waves) interact with surface currents at all scales due to a wide range of processes (Phillips, 1977). Except for very short fetch near the coast or for the shortest wave components, the growth of waves in the presence of winds is only significant over large scales, so that the local gradients in the dominant wave properties are generally dominated by current gradients(Phillips, 1984). In the ocean, it appears that refraction, which focuses wave energy in current jets that flow in the wave direction, is probably the dominant source of variations of wave heights at scales 50 to 200km with a minimal effect of wind gradients (Ardhuin et al., 2017). For currents speeds much weaker than the waves phase speed it is the rotational part of the current that is expected to explain the variations in wave directions (Landau & Lifshitz, 1960; Villas Bôas & Young, 2020). This refraction can lead

to extreme wave heights over large mesoscale currents, such as the Agulhas current, that are dangerous for ships and off-shore structures (Gutshabash & Lavrenov, 1986). Other impacts of waves on air-sea fluxes, upper ocean mixing or remote sensing also require better knowledge on wave-current interactions (e.g. D'Asaro, 2014; Sandwell et al., 2014; Villas Bôas et al., 2019).

Recent advances in understandings and in ocean modeling of surface ocean dynamic show that the upper ocean is highly energetic at the mesoscale, for which the flow is in quasi-geostrophic balance, but also at smaller scales (submesoscales) (McWilliams, 2016). Further, strong ocean currents are associated with sharp and asymetric velocity fronts, with larger positive vorticity maxima in the Northern hemisphere (e.g. Gula et al., 2015). Also, the generation of large surface waves has been shown to occur in the presence of strong internal waves (Osborne & Burch, 1980). All these small scale current features may contain as much surface kinetic energy (KE) as the mesoscales but it is not clear how much they influence the waves. Refraction theory tells us that changes in wave direction for a given wave frequency are the product of the current vorticity magnitude and the scale of the current feature, so that a localized high vorticity may have the same effect as a distributed but lower vorticity. But in practice, ocean waves are random and the different components of their relatively broad spectrum are affected in different ways by the surface vorticity.

The evolution of the wave field, represented by the wave action spectral densities $N(\sigma,\theta)$, with σ the wave frequency in the frame of reference moving with the local current and θ the wave propagation direction generally follows the wave action equation (Komen et al., 1994; Tolman & Booij, 1998),

$$\partial_t N + \partial_\lambda(\dot{\lambda}N) + \partial_\phi(\dot{\phi}N) + \partial_\sigma(\dot{\sigma}N) + \partial_\theta(\dot{\theta}N) = \frac{S}{\sigma} \tag{1}$$

The contributions of surface currents in equation (1) come into the advection speeds in longitude $\dot{\lambda}$ and latitude $\dot{\phi}$, which is the sum of the intrinsic group speed and the surface current, the refraction velocity $\dot{\theta}$, the change of frequency velocity $\dot{\sigma}$, and in the right-hand-side source term S because the effective wind velocity that generates waves is the vector difference of wind and surface current velocities (e.g., Ardhuin et al., 2017).

Because the effect of refraction $\dot{\theta}$ at position (λ,ϕ) combines with the advection in a new direction θ to produce a change in wave action N at another location (λ',ϕ'), there is no simple relationship between the current field and wave field, in other words, surface currents have a non local effect on the distribution of the wave action in the current field.

White and Fornberg (1998) have shown theoretically that the spatial distribution of refraction-induced focusing can be predicted for monochromatic waves over a random current with a narrow band spectrum. Still, that does not say much about the spatial distribution of wave heights in this case. The problem is more complex for broad band current spectrum and random waves, for which the significant wave height combines all the spectral components,

$$H_s = 4\sqrt{\int_0^\infty \int_0^{2\pi} \sigma N(\sigma,\theta)\mathrm{d}\theta\mathrm{d}\sigma}. \tag{2}$$

Guided by these theoretical insights and the solid foundation of the Wave Action Equation (e.g. White, 1999), our understanding of the effects of surface currents on wave height in the real ocean has relied on numerical simulations using eq. (1). These simulations are fairly successful for well-known tidal currents (e.g. Ardhuin et al., 2012), but there are very little data to validate modeled currents and waves in other regions. For example, wave simulations in the Gulf Stream and Drake Passage suggest

that the patterns of H_s field induced by surface currents is dominated by the refraction (Ardhuin et al., 2017), with a significant impact of small scale currents. These modelling results could not be validated using standard satellite altimeter data that is dominated by noise for along-track wavelengths shorter than 100km (Dibarboure et al., 2014). The development of new de-noising techniques has revealed a systematic relation between wave height gradients and current vorticity (Quilfen et al., 2018; Quilfen & Chapron, 2019). These filtered data have been compared to preliminary simulations in the Agulhas current using eq. (1) solved by either finite difference techniques or ray tracing. These comparisons have highlighted the importance of the directional width of the wave spectrum, with stronger H_s gradients obtained for narrower incident wave spectra even when only large scale currents, as derived from gridded altimetry data were used (Quilfen et al., 2018).

These two previous studies by Ardhuin et al. (2017) and Quilfen et al. (2018) have suggested two possible reasons for sharp H_s gradient: namely the presence of sharp current gradients, or the strong local focalisation of waves on a smooth current field. Figure 1 illustrates the first possibility over the Agulhas current, using either large-scale currents of gridded altimetry or a high resolution modeled current, both described in detail in section 2.

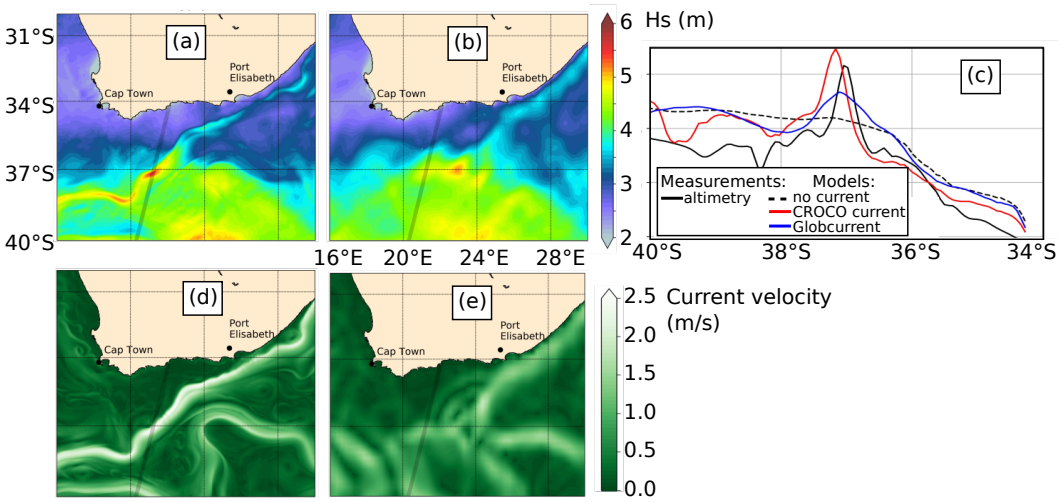

Figure 1. Snapshots of modeled H_s and surface current forcing in the Agulhas system for May 1^{st} 2016 at 15:00 UTC. Significant wave height (H_s) field computed with(a) the CROCO model(b) AVISO surface current. (c) Along-track significant wave height measured by altimeter. The solid black line is the measurement, the red and blue solid lines are H_s along the altimeter track computed with WW3 using different current forcing, CROCO or AVISO respectively. The dotted black line is the H_s simulated by the model without surface currents forcing. The position of the altimeter track and the H_s measurement are also shown on panels a,b,d,e. Surface current fields used in the model simulations are shown in (d) and (e).

The present work aims at consolidating these previous analyses and contribute to answering the questions: What are the parameters controlling the spatial variability of wave heights in a realistic current field? How can these be best reproduced by numerical models? In particular, we focus on the effect of the spatial resolution of the current field, and angular discretization of the wave model in relation with the directional spread of wave spectra. Here we focus on the Agulhas current because of

the strong H_s signature that is easily captured by satellite altimeters. Further work will be needed for other wave and current regimes.

The numerical model set up and data are presented in section 2. Results follow in section 3, with a discussion of the influence of the surface currents resolution in section 4. Finally we will conclude this wave-current interactions study in section 5.

2 Satellite and modelling data for waves in the Agulhas current

The Agulhas current system is one of the most intense western boundary currents, with velocities exceeding 2.5 m s^{-1} along the East coast of South Africa, before retroflecting back into the Indian Ocean with large ring eddies shed in the south Atlantic ocean (Beal et al., 2011; Tedesco et al., 2019). The Agulhas current system is also exposed to very large waves from the southern ocean (Young, 1999).

2.1 High-resolution altimetry H_s data

Satellite altimeters have been measuring H_s continuously for 27 years, providing measurements along sparsely spaced tracks, typically every 10 to 30 days (Ardhuin et al., 2019). In many regions of the ocean these are the only available measurement of wave heights. This is particularly the case in strong current regions where moored buoys are more difficult to install. Further, H_s measurements along the satellite ground track provide a unique view of the spatial variations of H_s, although along one dimension only. Until recently, the analysis of H_s variations was limited to wavelengths larger than 100 km, due to the noise associated to the tracking methods used to interpret altimeter waveforms (Sandwell et al., 2014; Ardhuin et al., 2017). The successful application of Empirical Mode Decomposition (Huang et al., 1998) to the denoising of H_s along-track series now makes it possible to investigate much smaller scales, possibly down to 15 km wavelength or less (Quilfen & Chapron, 2019). Here we use denoised wave heights from the European Space Agency (ESA) Sea State Climate Change Initiative (SeaState-CCI) version 1 database (Dodet et al., 2020), that uses this denoising technique applied to calibrated Geophysical Data Records from CNES and ESA for the Jason-2, Cryosat-2 and SARAL/AltiKa missions. The analysis of three years from 2014 to 2016 in our region of interest gives a total of 4746 satellite tracks, with one example shown in Fig. 1.

2.2 Numerical wave model

Our numerical wave model is based on the WAVEWATCH III modelling framework (The WAVEWATCH III® Development Group, 2016) that integrates the action balance equation (1), discretized on a regular latitude-longitude grid with a resolution of 1/30°. Our baseline configuration uses a spectral discretization into 32 frequencies from 0.037 Hz to 0.7 Hz and 48 directions ($\Delta\theta = 7.5°$). This model is forced by surface currents, as detailed below, together with operational hourly wind forecasts from the European Centre for Medium-Range Weather Forecasts (ECMWF), at 1/8° resolution. The overall time step used to solve eq. (1) is 390 s, and the solution is obtained with a splitting technique (Tolman, 1992), with a spatial advection step of 130 s, a refraction step of 18 s, and an automatically adjusted source term integration step that can be as short as 10 s. We define the boundaries with three hourly wave spectra from a global model configuration that uses the same wind fields but no current, a spatial resolution of 0.5° and the same spectral discretization as our Agulhas wave model. The wave model grid covers the domain shown in Fig. 1, from 40 to 30° S and 16 to 30° W.

The signature of the Agulhas systems is clearly visible in the modeled H_s field with a band of larger wave heights. On the example in Fig. 1.a, one can observe the effect of the main Agulhas current along the coast, including a meander known as a

"Natal pulse", located at 29°E, upstream of Port Elisabeth. Large current structures typically have multiple parallel branches caused by the straining of the large scale field and very sharp boundaries (Fig. 1.d). In contrast, the H_s field computed with the model using surface currents estimated from altimetry measurements (Globcurrent), has blurred patterns (Fig. 1.b), caused by surface currents with broader features and less intense maxima values (Fig. 1.e). The large scale circulation estimated from altimeter data although less energetic is coherent with the CROCO output snapshot: Agulhas current along the coast, retroflexion and Agulhas return current. For smaller scale features, all the 10–100km structures are missing in the Globcurrent product, including meanders of the Agulhas current along the coast, from 28° to E23°E which play an important role in the current stability (Tedesco et al., 2019). Also, the Agulhas current has a similar transport in both current fields but much sharper gradients and higher maxima, up to 3 m/s in the CROCO model result compared to 2 m/s in Globcurrent.

Altimeter measurements show a narrow H_s maximum around 37° in the Agulhas current upstream of the retroflexion (Fig. 1.c). This narrow peak in H_s is closer to the one obtained with the CROCO currents, while the Globcurrent current fields lead to a broad H_s maximum.

2.3 Currents fields used for forcing the wave model

Given the large influence of surface current details we have designed a series of simulations with currents at different resolutions. These current fields are based on surface current estimates from the Coastal and Regional Ocean COmmunity model (CROCO, Debreu et al., 2012) without data assimilation nor tidal forcing with a resolution of 1/36° both in latitude and longitude. The CROCO model domain is larger than the WW3 model domain that is shown in Fig. 1, and covers 15.1 33.7°E and 40.4 to 27.2°S. This CROCO model configuration is expected to produce surface currents that are statistically consistent with the real ocean and has been used for several process studies (Tedesco et al., 2019). However, for any particular time and location, the variable current structure is not expected to reproduce the stochastic behaviour of the ocean as no data assimilation is used within the model domain. The CROCO model has been forced at the surface by the ERA-interim reanalysis and boundaries have been forced by a global reanalysis GLORYS. We have also used low-pass filtered CROCO currents as an input forcing for the wave model. These are obtained by applying an isotropic two-dimensional Gaussian filter on both zonal and meridional components of the current velocity vector. This filter is defined by its standard deviation σ_c (fig 2a). We emphasize that the alternative approach of re-running CROCO at different resolutions may produce very different results and would require some tuning of each model configuration that is beyond the scope of the present work.

The filtered current fields effective resolution is the result of the convolution of the Gaussian filter and the original current field. Theoretically, the spectrum of the filtered current is the product of the original current spectrum and the spectrum of the Gaussian filter. In practice it means that the current spectrum rolls of sharply for wavelengths shorter than $L_c = 4\sigma_c$, or an effective resolution of $2\sigma_c$.

Seven surface currents fields have thereby been created, with effective resolutions ranging from 10 to 100km. Figure 3 illustrates four patterns of currents with the vorticity $\zeta = \partial V/\partial x - \partial U/\partial y$ and H_s corresponding to different current resolutions.

The filtering of the current field results in the removal of small scale structures, including small mesoscale eddies and filaments, as well as the smoothing of the large scale structures. Alternatively, we also used a surface current forcing taken from the Globcurrent product (Rio et al., 2014). This Globcurrent product has a spatial

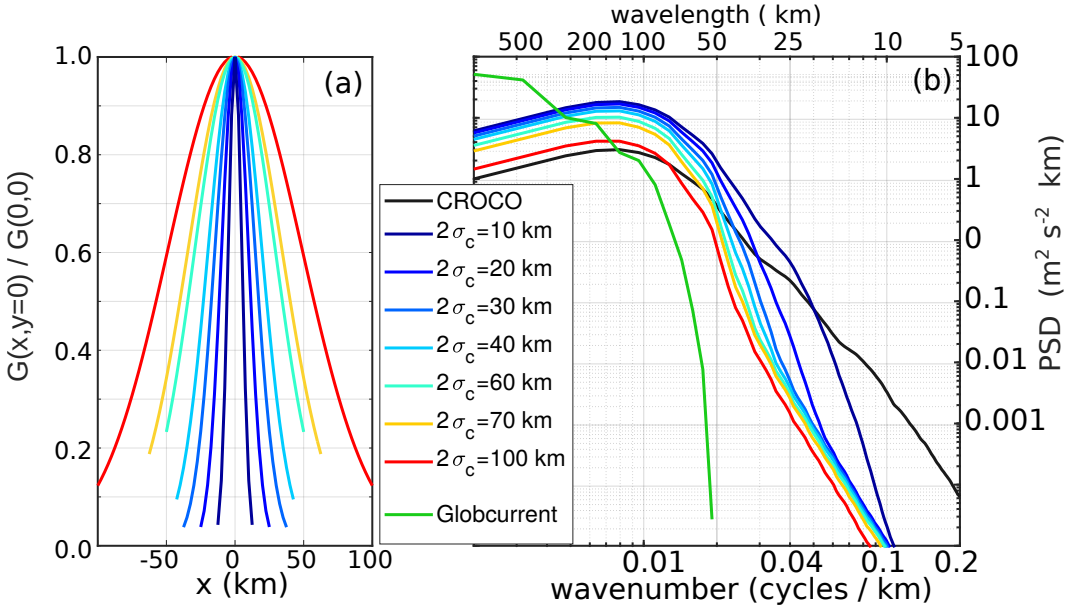

Figure 2. (a) Size and shape of the Gaussian filters G defined by their extent and the parameter σ_c. These are used to smooth the CROCO current fields. (b) Spectra of surface currents in the region 25.2–33.7°E 40.4–35.3°S, from the original and smoothed CROCO currents, and from Globcurrent.

resolution of 1/4° both in latitude and longitude and is temporally resolved at 1 day. It provides the geostrophic component of the total surface currents estimated from the Sea Surface Height (SSH) measured by altimeters, and a mean dynamic topography that combines other data sources (Rio et al., 2014). A similar spectral analysis described above has been applied on Globcurrent product and revealed its effective resolution 150km. The 60 km resolution filtered CROCO current has scales similar to those in the Globcurrent field, with a lower surface currents intensity for filtered surface current (due to filtering process). We note that the surface relative vorticity ζ of the filtered current (Fig. 3) is similar to the ones presented in figure 17c of Chelton et al. (2019) in the Coastal California current for similar resolution (few kilometers, 20km and 80km).

Snapshots of simulated H_s in Fig. (3a,b,c,d) illustrate how the wave height patterns follow the surface vorticity patterns as already shown in figure 13 of Quilfen et al. (2018). Figures (3 left) show a H_s maximum where the normalized vorticity is positive in the main stream of the Agulhas (southwestward) and also show that the H_s gradient is sharp for WW3 results forced with high resolution currents and become blurred for poorly resolved surface current. We have run our wave model during 3 years, from 2014 to 2016, with the appropriate surface currents (fully resolved from CROCO model, filtered and estimated by altimetry), wind and boundary conditions forcings.

3 Results

3.1 Spatial variability of H_s in realistic surface currents field

Wave-current interactions have been simulated in the Agulhas current from 2014 to 2016. Filtered altimetry data have been studied for the same time frame and all

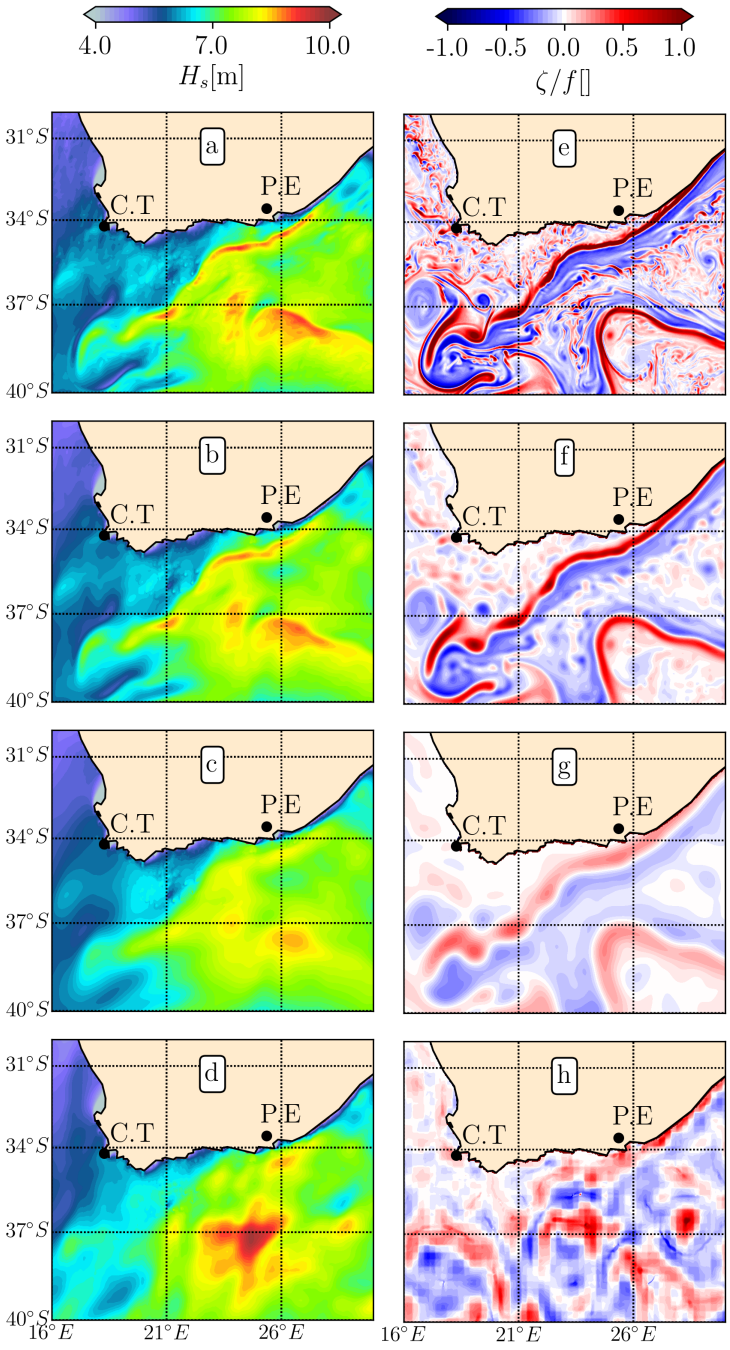

Figure 3. (a)-(d) snapshots of significant wave heights (H_s) in the Agulhas region simulated on 30$^{\text{th}}$ August 2015 at 00:00 UTC with a current forcing resolved at 2.5 km, 20 km, 60 km and 150 km (Globcurrent surface currents). (e)-(h) vertical normalized surface vorticity ζ=$\partial_x V \quad - \quad \partial_y U/f$, in the same area for currents resolved at 2.5 km , 20 km , 60 km and for Globcurrent product (150 km). We have used $f = 10^{-4}$ s^{-1} for the Coriolis parameter.

model outputs have been interpolated in time and space on those altimeters tracks. One example of model-satellite comparison is displayed 1c). Except for the topographically trapped flow patterns, the high resolution CROCO model is not expected to have current features in the same place as the real features, but it may still have realistic eddy sizes and meander shapes. We will thus compare the statisical properties of modeled and measured H_s.

In particular we consider the statistical properties of the along-track H_s gradient defined as

$$\nabla H_s = |\Delta H_s / dr|, \tag{3}$$

with dr the along-track distance between successive 1 Hz measurments (dr is typically 7 km), and ΔH_s the difference between successive H_s measurements taken 1 s apart. Statistics of ∇H_s have been interpolated on a regular grid with a resolution of 1/8° by 1/8° in longitude and latitude. The mean values are shown on figure 4, ranging from 0 to 3 cm per km.

A few high values of the H_s gradient right at the coast are clearly visible for the simulation without current. These high values can be explained by partial sheltering caused by headlands, all the large gradients appear in regions of strong current gradients, and specifically in the main Agulhas current, from 29°E 33°S to 17.5°E 39°S. The values of the mean ∇H_s measured in the main Agulhas branch are in the range of 1.5 to 3 cm/km (Fig. 4.i.) which is remarkably high, and corresponds to the maximum values shown in Figure 1. These persistent maximum gradients are located exactly where the model has the strongest current, and where the largest H_s gradients are also predicted in figure 4.a. This is the well known region of strong focalization of waves caused by wave refraction over the current (Gutshabash & Lavrenov, 1986; Kudryavtsev et al., 2017; Quilfen & Chapron, 2019). Indeed when propagating against a current that is uniform in the flow direction, waves of a given period and direction can be trapped: when coming from the center of the current towards its edge they turn back towards the center at the location where the current reaches a certain value (Kenyon, 1971). The waves behaviour is similar to the propagation of light waves along an optical fiber where light waves are trapped and propagate within a range of specific refraction's index values that depends on their initial incidence angle. Quilfen and Chapron (2019) have demonstrated with ray tracing and assuming the wave action is conserved along the ray, that where waves are trapped, strong ∇H_s are measured.

Figure 4 shows that the maximum ∇H_s signal is upstream 26°E, where the main Agulhas current is known to be stable. Downstream of 26°E the current is bi-modal with occasional disturbances known as Natal pulses

Around 22°E the Agulhas current comes off the Agulhas Bank and the current direction veers to the south, which probably explains the lower values of ∇H_s as the current direction is less favorable for trapping the dominant south-westerly waves, resulting in this lower gradient of wave heights. Beyond that point, ∇H_s increases again but it is more spread out in the north-south direction .

Nowhere does the much coarser and weaker current in the Globcurrent product produces H_s gradients larger than 2 cm/km (Fig. 4.g). Yet, the Globcurrent product leads to modeled gradients in the retroflexion region, around 38° S, 25 °E, that are similar to those given by the CROCO model, both weaker than observed. ∇H_s in the main Agulhas current are similar for CROCO filtered at 60km and Globcurrent, as shown in fig 3 through the H_s field. As the effective current resolution is degraded from 10km to 60km, the mean H_s gradient progressively vanishes with a particularly clear drop from 60 km (Fig. 4.e) to 70 km (Fig. 4.f). The magnitude of the gradients can be quantified by different percentiles, as shown in Fig. 5. For the 95th percentile and above, we find that 60% of the H_s gradient is obtained for effective current resolutions of 30 km or less.

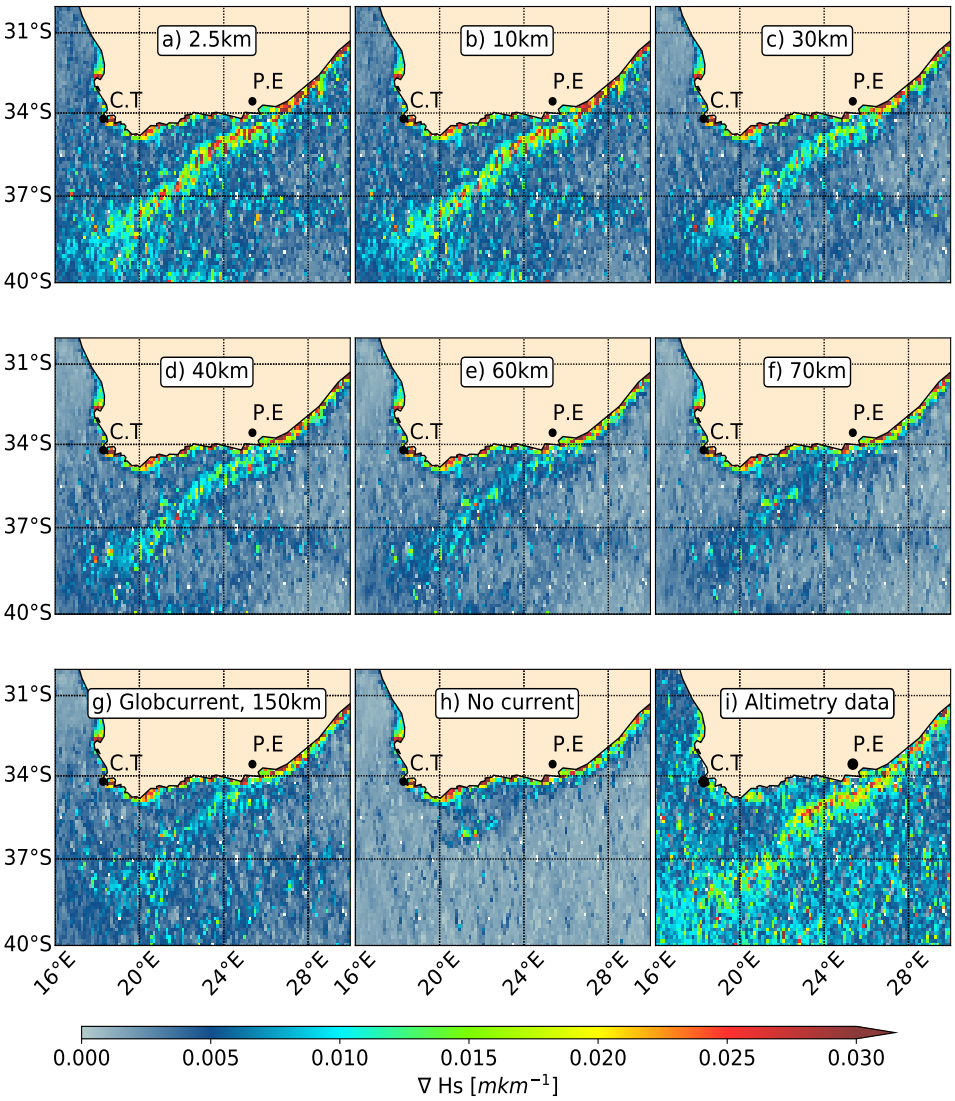

Figure 4. Significant wave height gradient (∇H_s) averaged over the years 2014–2016, from (a,b,c,d,e,f,g,h) model simulations and (i) altimeters data. ∇H_s estimated along satellite tracks are gridded on a regular 1/8° x 1/8° grid. Simulation with the original CROCO surface currents is represented in (a). Simulations forced with filtered surface currents at effective resolutions of 10km, 30km, 40km, 60km and 70km are displayed in panels b,c,d,e,f respectively. The simulation with Globcurrent data in shown in g) and the model result without any surface current forcing is shown in (h).

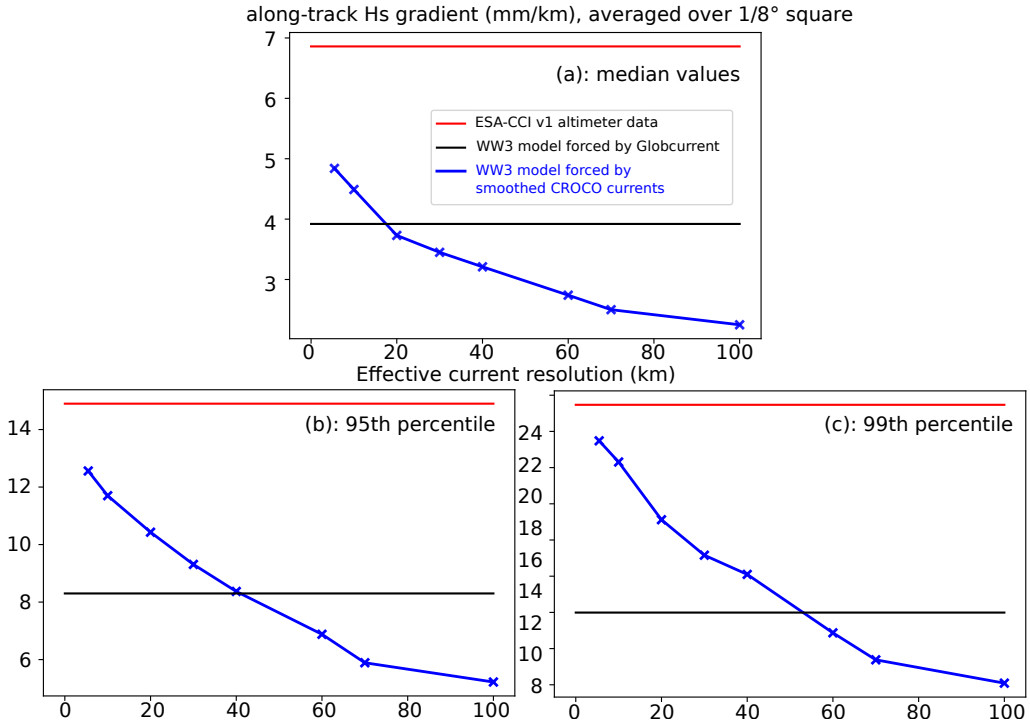

Figure 5. Statistics of the along-track gradients of H_s averaged on a grid for different model runs and for the satellite altimeter data. (a) Median, (b) 95th percentile, (c) 99th percentile.

3.2 Spectral analysis

In order to obtain a more quantitative analysis, we perform the same spectral analysis on the model and satellite data. We use overlapping windows following Welch (1967), with the Fourier transform computed after detrending and applying a Hanning window. Results are presented in Figure 6. In order to help with the interpretation, the surface current velocity ($\sqrt{U^2+V^2}$) was also analyzed along the same tracks. One spectrum is computed for each track. All spectra have been averaged to obtain one averaged spectrum for each numerical simulation for each surface currents forcing field. The H_s spectra (Fig. 6.a) show that between resolutions of 200 km and 30 km, and even down to the smaller resolved scale, the resolution of the surface currents drive the H_s variability. For wavelengths between 50 km and 100 km, simulations forced by the Globcurrent surface currents shows a H_s variability higher than simulations forced with surface currents filtered at 60km, 70km and 100km whereas surface currents from Globcurrent have an effective along-track resolution around 150km. This along-track resolution is consistent with the 150 to 250km resolution of sea surface height gridded altimeter data in the Agulhas region (Ballarotta et al., 2019).

Using a wave model forced by different surface current fields, fig. 6.b reveals what was already reported by Ardhuin et al. (2017), i.e the lower the surface currents KE ($<U>^2+<V>^2$, $<\,.\,>^2$ denotes the variable's variance), the lower the H_s spectrum. Surface KE spectrum computed from surface current taken from Globcurrent fields show a level of variability for wavelengths in the range 50 to 200km that is similar to the 40-km filtered current.

For all simulations, the shape of the spectrum of the modeled H_s is very similar to the KE spectrum, and slightly steeper, around $k^{-3.4}$ for H_s compared to $k^{-3.0}$ for the

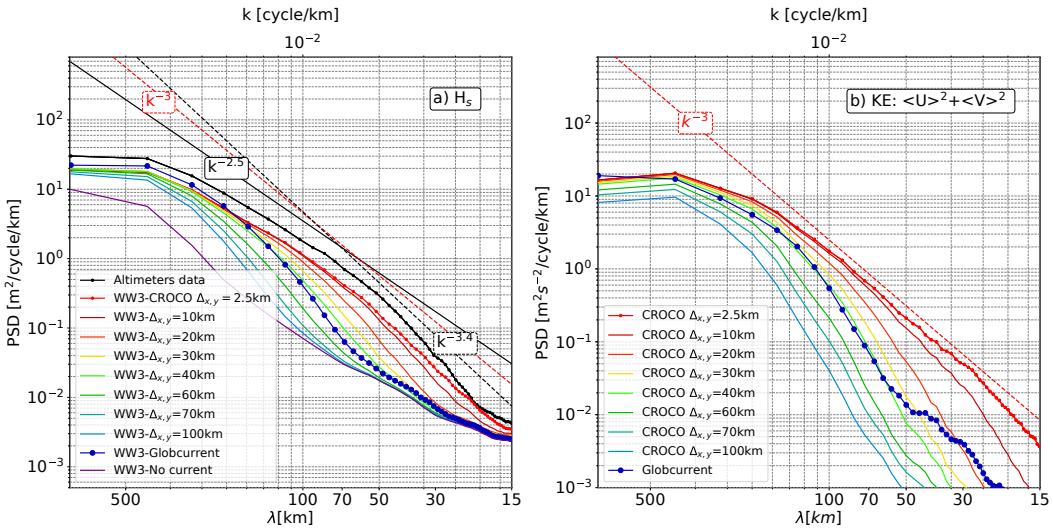

Figure 6. Left panel a), averaged Significant Wave Height spectra from model and altimetry data. Right panel b), averaged surface Kinetic Energy spectra. All spectra have been obtained by averaging all along-track spectra (4746 tracks) from altimeters measurements (black solid line) and interpolated simulated data (in colors). The associated surface currents resolution are given in the legend. λ is the wavelength.

KE spectrum (exponents have been computed through a linear regression) for scales smaller than 100 kilometers. The same behavior was found for realistic simulations in Gulf-Stream and Drake Passage (Ardhuin et al., 2017). As the spectral level in the current forcing is reduced, the H_s spectrum is reduced in the same proportion until it reaches a background level. For a wavelength of 100 km, this background level is around 0.08 m^2/cycle/km, which is very close to the variability associated to the wind field in the analysis by Ardhuin et al. (2017). This parallel behaviour of the H_s and KE spectra may be due to the dominant balance between propagation and refraction terms in the action balance equation (1).

4 Discussions and perspectives

4.1 Surface current resolution and gradients of H_s

In the ocean, surface currents are energetic at meso- and submesoscales, with features such as fronts, eddies and filaments. Waves interact with those features, and refraction explains the spatial redistribution of the wave action density that results in a change of H_s. In the Agulhas system, numerical wave simulations forced with highly resolved surface currents, rich in mesoscale structures show that the small features and sharp gradients are important for simulating realistic ∇H_s, statistically consistent with filtered altimeter data (Fig 5). We find that an effective resolution of 30 km, which resolves features with wavelengths larger than 60 km is necessary to reproduce most of the wave height gradients, which can be quantified by its median value or higher percentiles shown in Fig. 5. Given that the high resolution CROCO model that provides our forcing current does not assimilate observations, its features other than the largest scales of the Agulhas current are not expected to be in the right places at the right time, it is difficult to define a wave-gradient based metric that could be use to further validate the CROCO model for different regions or scales.

Quilfen et al. (2018) argued that the using a finite difference numerical wave model to solve the action balance eq. (1) generally underestimate the ∇H_s, showing marked differences between finite-differences and ray-tracing solutions. Here we find that it is the choice of a large scale current from Globcurrent that explains the relatively weak modeled H_s gradient.

4.2 Directional resolution in wave models

In the limit of a large number of directions and a fine spatial resolution, the solution to the wave action equation obtained here with third order finite-difference refraction and advection schemes (Leonard, 1991; Tolman, 2002) should be identical to the one obtained with backward ray tracing (Longuet-Higgins, 1957; O'Reilly & Guza, 1993; Booij et al., 1999; Ardhuin & Herbers, 2005). In practice, the number of discrete model directions is limited by the cost in memory storage and computation time, and most wave model implementations use 24 to 36 directions. Given the importance of refraction in the presence of current gradients (Holthuijsen & Tolman, 1991; Ardhuin et al., 2012), we used 48 directions in the analysis presented above. We examine here the importance of the directional resolution and how the numerical solution is smoothed by the use of a small number of directions. We have thus repeated our simulations (same forcing files and same boundary conditions) different directional resolutions ($\Delta\theta$), using 24 ($\Delta\theta = 15°$), and 180 ($\Delta\theta = 2°$) directions instead of 48 ($\Delta\theta = 7.5°$). The refraction timestep Δt_r has been changed in proportion to keep a constant ratio $\Delta t_r/\Delta\theta$. We have further checked than reducing the other time steps had minimal effects on the solution. The spectral analysis described in section (3.2) has been repeating for those new simulations and presented in figure (7 a). Because the $\Delta\theta = 2°$ simulation is extremely costly, the wave model has been run for 4 months only, from the 1^{st} January to the 30^{st} April 2015. The altimeters track have been extracted for the same time frame and the model outputs have been interpolated on those tracks.

Spectral analysis shows that the model set-up with a finer directional resolution ($N_\theta = 48$ instead of 24) has a larger variability of H_s at all scales, with an increase of the PSD by about a factor of 2, similar to what was found for Drake passage by Ardhuin et al. (2017). In addition, for scales smaller than 100km, H_s variability is stronger for simulations forced with higher resolution currents. Further refining the directional resolution to 180 directions gives a further increase in H_s variability. When the narrow directional discretization is combined with high resolution currents, the modeled H_s spectrum is within 30% of the satellite measurements for all scales shorter than 100 km.

A typical example of spatial variability along a transect is shown in (Fig. 7.b,c), with a much sharper peak of H_s in the model runs using 180 or 48 directions.

4.3 Influence of incident waves directional spreading (σ_θ)

We generally expect that a fine directional resolution is most important when the directional wave spectrum is very narrow. In these conditions, wave energy can be focused in a small area, as predicted by the analysis of monochromatic waves with rays traced with parallel directions outside of the current region (White & Fornberg, 1998). In contrast, broad wave spectra have focal points in different locations for the different spectral components, which effectively smears the regions of maximum H_s.

In order to quantify that effect in realistic conditions, we have re-run the model with modified boundary conditions. Instead of taking the directional wave spectra $E(f, \theta)$ straight from a global hindcast, we now make these spectra broader or narrower in directions, without changing the spreading along the frequency nor the mean

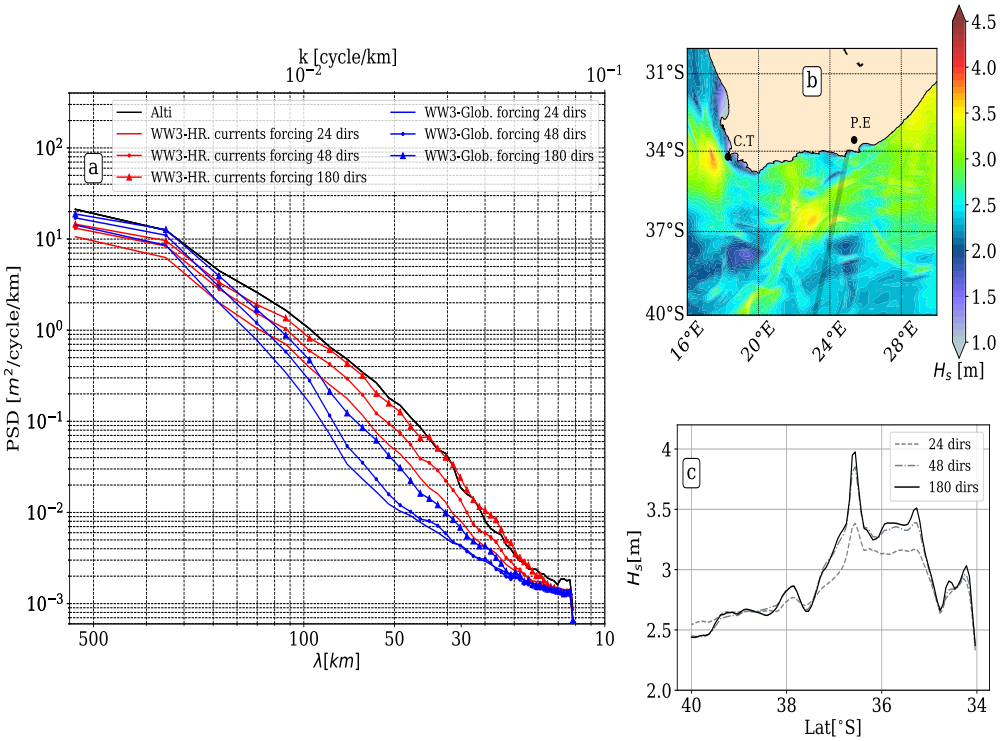

Figure 7. a) panel: Averaged Significant Wave Height spectra for altimeters measurements (in black) and for modeled data (colors). Blue spectra are for modeled wave height forced with surface current from Globcurrent (Glob.) and red spectra for high resolved (HR) CROCO forcing. b) instantaneous simulated significant wave height field highly resolved in directions (180 dirs). c) an example of modeled wave heights interpolated along an altimeter track for different directional resolution, the location of the track is in black line on panel b). λ is the wavelength.

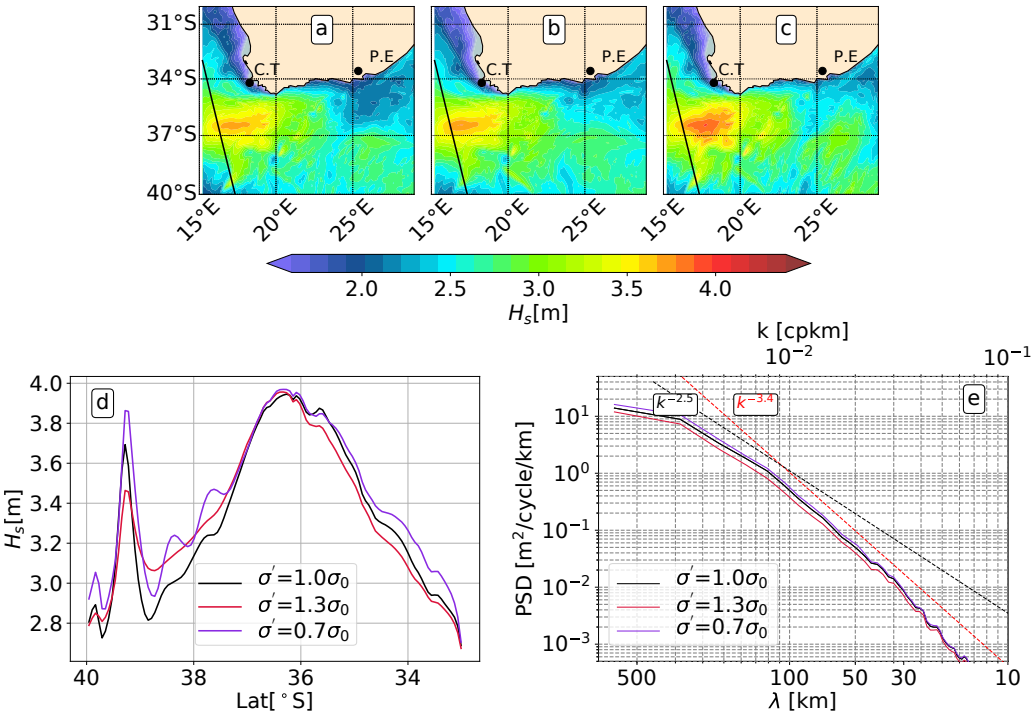

Figure 8. Up figures, two dimensional significant wave height field snapshot (November 4ˆth 00:00 UTC) for: a) the unchanged directional spreading (σ_θ) boundary spectra, b) the extended σ_θ boundary spectra (+30%), c) the reduced σ_θ boundary spectra (-30%). The solid line is the footprint of one altimeter track for the same date, the significant waves height simulated are displayed on the d) panel for unmodified (black line), extended (red line) and reduced (purple line) σ_θ. The e) panel shows the averaged simulated H_s spectra over one year for the three simulations.

direction at each frequency. The details of the method are given in the Appendix. The conservation of the total variance and mean direction between all original spectra and new spectra has been verified. At each frequency, the original directional spreading has been changed by ±30%. Examples of the resulting H_s fields are displayed on Figure 8.a-c. Figure 8 illustrates how a decrease of σ_θ induce an increase in the number of small H_s structures and an amplification of structures already existing, and vice versa. This is better quantified along a track that is close to the upwave (western) boundary. The left peak at 39.5° S in Fig.8.d has a variation of H_s from 3.45m with a broader spectrum to 3.85 m with a narrower spectrum. This 25% change in wave energy is a typical order of magnitude. Besides the peak, some fluctuations of H_s between 37 and 39° S are much reduced for the broader spectra.

Following the method used previously, we now look at the averaged H_s spectra for each 1-year long simulation, with different boundary conditions. The result shows higher variability, by about 50%, at all scales for incident waves with lower values of the directional spread σ_θ. The shape of the H_s spectra are very similar for all simulations with a steeper slope for wavelenghts shorter than 125 km.

Our simulations have confirmed that over a real current system like the Agulhas, the spatial variability is sensitive to the spectral width of the wave field, and to the numerical resolution used in models with narrower spectra and finer resolution producing stronger gradients. Unfortunately the directional spread is one of the worst

modeled parameters (Stopa et al., 2016). More directional data, such as provided by the SWIM instrument on the China France Ocean Satellite (Hauser et al., 2017), may help design better model parameterizations and can be used for data assimilation with important impact in strong current regions.

5 Conclusion

Surface currents modify the wave field in a complex way that is not just local (White & Fornberg, 1998; Ardhuin et al., 2017; Kudryavtsev et al., 2017), creating a spatial pattern of wave properties that can be important for applications and that may reveal properties of the ocean currents that are otherwise difficult to obtain. Large mesoscale current systems such as the Agulhas current are places where particularly strong H_s gradients are found (Lavrenov, 1998; Quilfen & Chapron, 2019). Combining state of the art of wave modelling and novel filtered altimetry data, we have investigated the factors that lead to these large gradients, and under which conditions they can be reproduced by numerical models. The present work shows that model forced with realistic and high resolved surface currents, statistically consistent with the real upper ocean dynamics and sufficiently discretized in direction, is able to capture sharp significant wave height gradient measured by satellite altimeters. These sharp gradients are much reduced in the results of wave models that are forced by surface currents derived from a combination of mean dynamic topography (Rio et al., 2014) and sea level anomalies derived from these same altimeters that measure the wave heights. This low resolution of satellite-derived currents (Ballarotta et al., 2019; Chelton et al., 2019), is related to the sparse tracks of existing and planned nadir altimeters, but it is also due to the along-track noise level in the processing used today for altimeter data.

Besides the structures of the forcing current, the numerical implementations of wave models will typically miss part of the true gradients of the wave field due to numerical diffusion. Here we find that high spectral resolutions, using 48 or more directions systematically produces finer details, in a way that is statistically consistent with altimeter data. This effect is most pronounced when the directional wave spectrum is most narrow. Reproducing realistic wave height gradients is important for marine safety but also for studying upper ocean processes driven by wave breaking. It is also a necessity to capture sea states biases in ocean remote sensing of wide range of variables, from sea level (Minster et al., 1991) to sea surface salinity (Reul & Chapron, 2003) or surface currents (Ardhuin et al., 2018; Marié et al., 2020).

We found that the gradients of significant wave heights can be quantified in satellite altimeter data in a way that is useful to make a statement on the quality of the ocean currents, in the context of numerical wave modelling. We can imagine that many future developments will further constrain the currents by using 1) more information about the wave field than just the wave height 2) measurements over a broader area than the narrow pencil beam of nadir altimeters, 3) different analyses and techniques. For the first type of future developments, we can mention the use of directional measurements provided by the China France Ocean Satellite (Hauser et al., 2017), launched in October 2018, and the understanding of directional spectral evolution in currents provided by (Villas Bôas & Young, 2020). For the second aspect, we are expecting a wealth of data, including wave measurements, from the soon-to-be-launched Surface Water Ocean Topography mission (Morrow et al., 2019). As for the third aspect it can involve the use of different metrics. For example, (Villas Bôas et al., 2020) showed that the magnitude of the wave height gradient was also related to the slope of the current kinetic energy spectrum, which is an interesting quantity for diagnosing the upper ocean dynamics (Le Traon et al., 2008).

Appendix: Defining new waves spectrum with a modified directional spreading

We force the wave model at its boundaries with bi-dimensional wave spectra from a global hindcast forced without current, $E(f,\theta)$ with f the wave intrinsic frequency and θ the direction where energy is propagating. Two-dimensional wave spectrum can be divided in an omnidirectional spectrum $E(f)$ and a directional shape function $D(f,\theta)$ defined as

$$D(f,\theta) = \frac{E(f,\theta)}{E(f)} \tag{4}$$

such that

$$\int_0^{2\pi} D(f,\theta)\mathrm{d}\theta = 1. \tag{5}$$

Our modification of the boundary conditions is done by a modification of $D(f,\theta)$, without changing $E(f)$.

There can be an infinite number of ways to modify $D(f,\theta)$. Here first compute the directional moments $a_1(f)$, $b_1(f)$, $a_2(f)$, $b_2(f)$ are computed from $D(f,\theta)$ following O'Reilly et al. (1996). These are the discrete Fourier coefficients of the directional distribution $D(f,\theta)$.

From these moments, the following directional parameters have been computed.

$$\begin{cases} \theta_1 = \arctan(b_1/a_1) & \text{(6.a)} \\ \theta_2 = \dfrac{1}{2}\arctan(b_2/a_2) & \text{(6.b)} \\ \sigma_1 = 2\left(1 - \sqrt{a_1^2 + b_1^2}\right) & \text{(6.c)} \\ \sigma_2 = \dfrac{1}{2}\left(1 - \sqrt{a_2^2 + b_2^2}\right) & \text{(6.d)} \end{cases}$$

Both directional spreads $\sigma_1(f)$ and $\sigma_2(f)$ are multiplied by a parameter α, giving $\sigma_1'(f)$ and $\sigma_2'(f)$.

From the modified parameters, a new directional distribution $D'(f,\theta)$ is estimated using the the Maximized Entropy Method (Lygre & Krogstad, 1986).

Acknowledgments

G.M. is supported by Centre National de l'Etude Spatiale (CNES) and by the Region Bretagne through l'Allocations de recherche doctorale (ARED). Filtered altimeter data are from the European Space Agency Climate Change Initiative Sea State v1 dataset and is freely available on the ESA CCI website (http://cci.esa.int/data) at `ftp://anon-ftp.ceda.ac.uk/neodc/esacci/sea_state/data/v1.1_release`. Surface currents derived from altimeters (Globcurrent product) are available in NetCDF format at `ftp://ftp.ifremer.fr/ifremer/ww3/FORCING/GLOBCURGEO/NC4/`. The surface currents simulation from CROCO fully resolved were kindly provided by P. Penven (WOES, Western indian Ocean Energy Sink) and performned as part of the GENCI/IDRIS grant A0040107630. Both fully resolved currents and filtered currents are available at `ftp://ftp.ifremer.fr/ifremer/ww3/FORCING/CROCO/CROCO_AGULHAS/NC4/` in NetCDF format. Authors also thanks M. Accensi for his contribution to the development and maintenance of the WAVEWATCH III model.

References

Ardhuin, F., Aksenov, Y., Benetazzo, A., Bertino, L., Brandt, P., Caubet, E., ... Xie, J. (2018). Measuring currents, ice drift, and waves from space: the sea surface kinematics multiscale monitoring (SKIM) concept. *Ocean Sci.*, *14*, 337–354. doi: 10.5194/os-2017-65

Ardhuin, F., Dumas, F., Bennis, A.-C., Roland, A., Sentchev, A., Forget, P., ... Benoit, M. (2012). Numerical wave modeling in conditions with strong currents: dissipation, refraction and relative wind. *J. Phys. Oceanogr.*, *42*, 2101–2120.

Ardhuin, F., & Herbers, T. H. C. (2005). Numerical and physical diffusion: Can wave prediction models resolve directional spread? *J. Atmos. Ocean Technol.*, *22*(7), 886–895. Retrieved from `http://journals.ametsoc.org/doi/pdf/10.1175/JTECH1723.1`

Ardhuin, F., Rascle, N., Chapron, B., Gula, J., Molemaker, J., Gille, S. T., ... Rocha, C. (2017). Small scale currents have large effects on wind wave heights. *J. Geophys. Res.*, *122*(C6), 4500–4517. doi: 10.1002/2016JC012413

Ardhuin, F., Stopa, J. E., Chapron, B., Collard, F., Husson, R., Jensen, R. E., ... Young, I. (2019). Observing sea states. *Frontiers in Marine Sci.*, *6*, 124. doi: 10.3389/fmars.2019.00124

Ballarotta, M., Ubelmann, C., Pujol, M.-I., Taburet, G., Fournier, F., Legeais, J.-F., ... Picot, N. (2019). On the resolutions of ocean altimetry maps. *Ocean Science Discussions*. doi: 10.5194/os-2018-156

Beal, L. M., Ruijter, W. P. M. D., Biastoch, A., Zahn, R., Cronin, M., Hermes, J., ... Zinke, J. (2011). On the role of the agulhas system in ocean circulation and climate. *Nature*, *472*, 429–436. doi: doi:10.1038/nature09983

Booij, N., Ris, R. C., & Holthuijsen, L. H. (1999, April). A third-generation wave model for coastal regions. 1. model description and validation. *J. Geophys. Res.*, *104*(C4), 7,649–7,666.

Chelton, D. B., Schlax, M. G., Samelson, R. M., Farrar, J. T., Molemaker, M. J., McWilliams, J. C., & Gula, J. (2019). Prospects for future satellite estimation of small-scale variability of ocean surface velocity and vorticity. *Progress in Oceanography*, *173*, 256–350. doi: 10.1016/j.pocean.2018.10.012

D'Asaro, E. A. (2014). Turbulence in the upper-ocean mixed layer. *Annu. Rev. Mar. Sci.*, *6*, 101–115. doi: 10.1146/annurev-marine-010213-135138

Debreu, L., Marchesiello, P., Penven, P., & Cambon, G. (2012). Two-way nesting in split-explicit ocean models: Algorithms, implementation and validation. *Ocean Modelling*, *49*, 1–21. doi: 10.1016/j.ocemod.2012.03.003

Dibarboure, G., Boy, F., Desjonqueres, J. D., Labroue, S., Lasne, Y., Picot, N., ... Thibaut, P. (2014). Investigating short-wavelength correlated errors on low-resolution mode altimetry. *J. Atmos. Ocean Technol.*, *31*, 1337–1362. doi: 10.1175/JTECH-D-13-00081.1

Dodet, G., Piolle, J.-F., Quilfen, Y., Abdalla, S., Accensi, M., Ardhuin, F., ... Donlon, C. (2020). The sea state cci dataset v1: towards a sea state climate data record based on satellite observations. *Earth System Sci. Data*, *12*, 1929–1951. doi: 10.5194/essd-12-1929-2020

Gula, J., Molemaker, M. J., & Mcwilliams, J. C. (2015). Gulf stream dynamics along the southeastern u.s. seaboard. *J. Phys. Oceanogr.*, *45*, 690–715.

Gutshabash, Y. S., & Lavrenov, I. V. (1986). Swell transformation in the cape Agulhas current. *Izv. Atmos. Ocean. Phys.*, *22*(6), 494–497.

Hauser, D., Tison, C., Amiot, T., Delaye, L., Corcoral, N., & Castillan, P. (2017). SWIM: The first spaceborne wave scatterometer. *IEEE Trans. on Geosci. and Remote Sensing*, *55*(5), 3000–3014.

Holthuijsen, L. H., & Tolman, H. L. (1991, July). Effects of the Gulf Stream on ocean waves. *J. Geophys. Res.*, *96*(C7), 12755–12771.

Huang, N. E., Shen, Z., Long, S. R., Wu, M. C., Shih, H. H., Zheng, Q., ... Liu, H. H. (1998). The empirical mode decomposition and the Hilbert spectrum for nonlinear and non-stationary time series analysis. *Proc. Roy. Soc. Lond. A*, *454*, 903–995.

Kenyon, K. E. (1971). Wave refraction in ocean current. *Deep Sea Res.*, *18*.

Komen, G. J., Cavaleri, L., Donelan, M., Hasselmann, K., Hasselmann, S., & Janssen, P. A. E. M. (1994). *Dynamics and modelling of ocean waves*. Cambridge: Cambridge University Press.

Kudryavtsev, V., Yurovskaya, M., Chapron, B., Collard, F., & Donlon, C. (2017). Sun glitter imagery of surface waves. part 2: Waves transformation on ocean currents. *J. Geophys. Res.*, *122*. doi: 10.1002/2016JC012426

Landau, L. D., & Lifshitz, E. M. (1960). *Mechanics*. Reading, MA: Pergamon Press Addison-Wesley.

Lavrenov, I. V. (1998). The wave energy concentration at the Agulhas Current off South Africa. *Nat. Hazards*, *17*, 117–127.

Leonard, B. P. (1991). The ULTIMATE conservative difference scheme applied to unsteady one-dimensional advection. *Computational Methods in Applied Mechanical Engineering*, *88*, 17–74.

Le Traon, P.-Y., Klein, P., Hua, B. L., & Dibarboure, G. (2008). Do altimeter wavenumber spectra agree with the interior or surface quasigeostrophic theory? *J. Phys. Oceanogr.*, *38*, 1137–1142.

Longuet-Higgins, M. S. (1957). On the transformation of a continuous spectrum by refraction. *Proceedings of the Cambridge philosophical society*, *53*(1), 226–229.

Lygre, A., & Krogstad, H. E. (1986). Maximum entropy estimation of the directional distribution in ocean wave spectra. *J. Phys. Oceanogr.*, *16*, 2,052–2,060.

Marié, L., Collard, F., Nouguier, F., Pineau-Guillou, L., Hauser, D., Boy, F., ... Ardhuin, F. (2020). Measuring ocean surface velocities with the kuros airborne near-nadir doppler radar: a multi-scale analysis in preparation of the skim mission. *Ocean Sci.*, *16*, 1399–1429. doi: 10.5194/os-16-1399-2020

McWilliams, J. C. (2016). Submesoscale currents in the ocean. *Proc. R. Soc. A*, *427*, 20160117. doi: 10.1098/rspa.2016.0117

Minster, J. F., Jourdan, D., Boissier, C., & Midol-Monnet, P. (1991). Estimation of the sea-state bias in radar altimeter Geosat data from examination of frontal systems. *J. Atmos. Ocean Technol.*, *9*, 174–187.

Morrow, R., Fu, L.-L., Ardhuin, F., Benkiran, M., Chapron, B., Cosme, E., ... Zaron, E. D. (2019). Global observations of fine-scale ocean surface topography with the Surface Water and Ocean Topography (SWOT) mission. *Frontiers in Marine Sci.*, *6*, 232. doi: 10.3389/fmars.2019.00232

O'Reilly, W. C., & Guza, R. T. (1993). A comparison of two spectral wave models in the Southern California Bight. *Coastal Eng.*, *19*, 263–282.

O'Reilly, W. C., Herbers, T. H. C., Seymour, R. J., & Guza, R. T. (1996). A comparison of directional buoy and fixed platform measurements of Pacific swell. *J. Atmos. Ocean Technol.*, *13*, 231–238.

Osborne, A. R., & Burch, T. L. (1980). Coupling between a surface-wave spectrum and an internal wave: modulation interaction. *Science*, *208*(4443), 513–460.

Phillips, O. M. (1977). *The dynamics of the upper ocean*. London: Cambridge University Press. (336 p.)

Phillips, O. M. (1984). On the response of short ocean wave components at a fixed wavenumber to ocean current variations. *J. Phys. Oceanogr.*, *14*, 1425–1433. Retrieved from `https://journals.ametsoc.org/doi/abs/10.1175/1520-0485%281984%29014%3C1425%3AOTROSO%3E2.0.CO%3B2` doi: 10.1175/1520-0485(1984)014⟨1425:OTROSO⟩2.0.CO;2

Quilfen, Y., & Chapron, B. (2019). Ocean surface wave-current signatures from satellite altimeter measurements. *Geophys. Res. Lett.*, *216*, 253-261. doi: 10.1029/2018GL081029

Quilfen, Y., Yurovskaya, M., Chapron, B., & Ardhuin, F. (2018). Storm waves sharpening in the Agulhas current: satellite observations and modeling. *Remote sensing of Environment*, *216*, 561-571. doi: 10.1016/j.rse.2018.07.020

Reul, N., & Chapron, B. (2003). A model of sea-foam thickness distribution for passive microwave remote sensing applications. *J. Geophys. Res.*, *108*(C10), 3321. doi: 10.1029/2003JC001887

Rio, M.-H., Mulet, S., & Picot, N. (2014). Beyond GOCE for the ocean circulation estimate: Synergetic use of altimetry, gravimetry, and in situ data provides new insight into geostrophic and Ekman currents. *Geophys. Res. Lett.*, *41*, 8918–8925. doi: 10.1002/2014GL061773

Sandwell, D. T., Müller, R. D., Smith, W. H. F., Garcia, E., & Francis, R. (2014). New global marine gravity model from cryosat-2 and Jason-1 reveals buried tectonic structure. *Science*, *346*, 65–67. doi: 10.1126/science

Stopa, J. E., Ardhuin, F., Bababin, A., & Zieger, S. (2016). Comparison and validation of physical wave parameterizations in spectral wave models. *Ocean Modelling*, *103*, 2–17. doi: 10.1016/j.ocemod.2015.09.003

Tedesco, P., Gula, J., Ménesguen, C., Penven, P., & Krug, M. (2019). Generation of submesoscale frontal eddies in the agulhas current. *Journal of Geophysical Research*, *124*, 7606–7625. doi: 10.1029/2019JC015229

The WAVEWATCH III® Development Group. (2016). *User manual and system documentation of WAVEWATCH III ® version 5.16* (Tech. Note No. 329). College Park, MD, USA: NOAA/NWS/NCEP/MMAB. (326 pp. + Appendices)

Tolman, H. L. (1992). Effects of numerics on the physics in a third-generation wind-wave model. *J. Phys. Oceanogr.*, *22*, 1095–1111. Retrieved from `http://journals.ametsoc.org/doi/pdf/10.1175/1520-0485%281992%29022%3C1095%3AEONOTP%3E2.0.CO%3B2`

Tolman, H. L. (2002). Limiters in third-generation wind wave models. *Global Atmos. Ocean Syst.*, *8*, 67–83.

Tolman, H. L., & Booij, N. (1998). Modeling wind waves using wavenumber-direction spectra and a variable wavenumber grid. *Global Atmos. Ocean Syst.*, *6*, 295–309.

Villas Bôas, A. B., Ardhuin, F., Gommenginger, C., Rodriguez, E., Gille, S. T., Cornuelle, B. D., ... Tsamados, M. (2019). Integrated observations and modeling of winds, currents, and waves: requirements and challenges for the next decade. *Frontiers in Marine Sci.*, *6*, 425. doi: 10.3389/fmars.2019.00425

Villas Bôas, A. B., Cornuelle, B. D., Mazloff, M. R., Gille, S. T., & Ardhuin, F. (2020). Wave-current interactions at meso and submesoscales: Insights fromidealized numerical simulations. *J. Phys. Oceanogr., in press*. doi: 10.1002/2016JC012413

Villas Bôas, A. B., & Young, W. R. (2020). Integrated observations and modeling of winds, currents, and waves: requirements and challenges for the next decade. *J. Fluid Mech.*, *890*, R3. doi: 10.1017/jfm.2020.116

Welch, P. D. (1967). The use of fast Fourier transform for the estimation of power spectra: a method based on time averaging over short, modified periodograms. *IEEE Trans. Audio and Electroacoustics*, *15*(2), 70–73.

White, B. S. (1999). Wave action on currents with vorticity. *J. Fluid Mech.*, *386*, 329–344.

White, B. S., & Fornberg, B. (1998). On the chance of freak waves at sea. *J. Fluid Mech.*, *355*, 113–138.

Young, I. R. (1999). *Wind generated ocean waves*. Oxford: Elsevier Science.